ACS NANOSCIENCE Au
AN OPEN ACCESS JOURNAL OF THE AMERICAN CHEMICAL SOCIETY

pubs.acs.org/nanoau
Article

Interband and Intraband Hot Carrier-Driven Photocatalysis on Plasmonic Bimetallic Nanoparticles: A Case Study of Au–Cu Alloy Nanoparticles

Published as part of ACS Nanoscience Au special issue "Advances in Energy Conversion and Storage at the Nanoscale".

Mengqi Sun, Ankai Wang, Min Zhang, Shengli Zou, and Hui Wang*

Cite This: ACS Nanosci. Au 2024, 4, 360–373

Read Online

ACCESS | Metrics & More | Article Recommendations | Supporting Information

ABSTRACT: Photoexcited nonthermal electrons and holes in metallic nanoparticles, known as hot carriers, can be judiciously harnessed to drive interesting photocatalytic molecule-transforming processes on nanoparticle surfaces. Interband hot carriers are generated upon direct photoexcitation of electronic transitions between different electronic bands, whereas intraband hot carriers are derived from nonradiative decay of plasmonic electron oscillations. Due to their fundamentally distinct photogeneration mechanisms, these two types of hot carriers differ strikingly from each other in terms of energy distribution profiles, lifetimes, diffusion lengths, and relaxation dynamics, thereby exhibiting remarkably different photocatalytic behaviors. The spectral overlap between plasmon resonances and interband transitions has been identified as a key factor that modulates the interband damping of plasmon resonances, which regulates the relative populations, energy distributions, and photocatalytic efficacies of intraband and interband hot carriers in light-illuminated metallic nanoparticles. As exemplified by the Au–Cu alloy nanoparticles investigated in this work, both the resonant frequencies of plasmons and the energy threshold for the *d*-to-*sp* interband transitions can be systematically tuned in bimetallic alloy nanoparticles by varying the compositional stoichiometries and particle sizes. Choosing photocatalytic degradation of Rhodamine B as a model reaction, we elaborate on how the variation of the particle sizes and compositional stoichiometries profoundly influences the photocatalytic efficacies of interband and intraband hot carriers in Au–Cu alloy nanoparticles under different photoexcitation conditions.

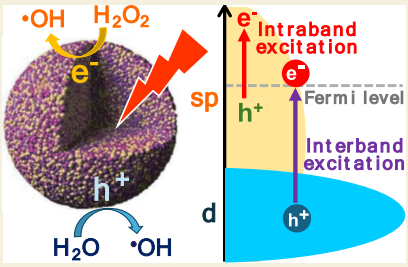

KEYWORDS: *plasmon resonances, interband transitions, hot carriers, photocatalysis, bimetallic nanoparticles, alloys*

INTRODUCTION

Optically excited metallic nanoparticles exhibit intriguing photocatalytic behaviors, efficaciously converting solar energy into chemical energy through hot carrier-driven molecular transformations.[1−6] The photoexcited hot carriers exploitable for photocatalysis can be created in metallic nanoparticles through two fundamentally distinct mechanisms, nonradiative plasmon decay and interband electronic transitions.[7−12] In the context of classical electromagnetic theory, plasmons can be described as collective oscillations of free electrons in resonance with the oscillating electric fields of incident light. Resonantly excited plasmons only maintain their coherence for approximately 1−10 fs, undergoing rapid decay either radiatively through elastic photon scattering or nonradiatively through Landau damping, in which electron–hole pairs with energy distributions far from the thermal equilibrium are generated.[2−5,7] Landau damping can be described as a pure quantum mechanical process in which a plasmon quantum decays into an intraband electronic transition between filled and empty states within the conduction band of the material.[2] Therefore, the nonthermal charge carriers derived from Landau damping are commonly referred to as intraband hot carriers. In contrast, interband hot carriers can be excited in a photoilluminated metallic nanoparticle upon direct electronic transitions between different bands when the excitation photon energies exceed the threshold required for such interband transitions.[7,8,11−14]

Interband and intraband hot carriers differ vastly from each other in terms of their lifetimes, energy distribution profiles, mean free paths, and relaxation dynamics,[7,8,11] all of which are key factors profoundly influencing not only the photocatalytic efficiencies but also the reaction outcomes. While plasmonic photocatalysis driven by intraband hot carriers has been intensively investigated in the past two decades,[1−6] utilization

Received: June 25, 2024
Revised: August 18, 2024
Accepted: August 26, 2024
Published: August 30, 2024

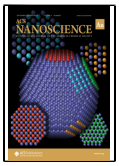

https://doi.org/10.1021/acsnanoscienceau.4c00035
ACS Nanosci. Au 2024, 4, 360–373

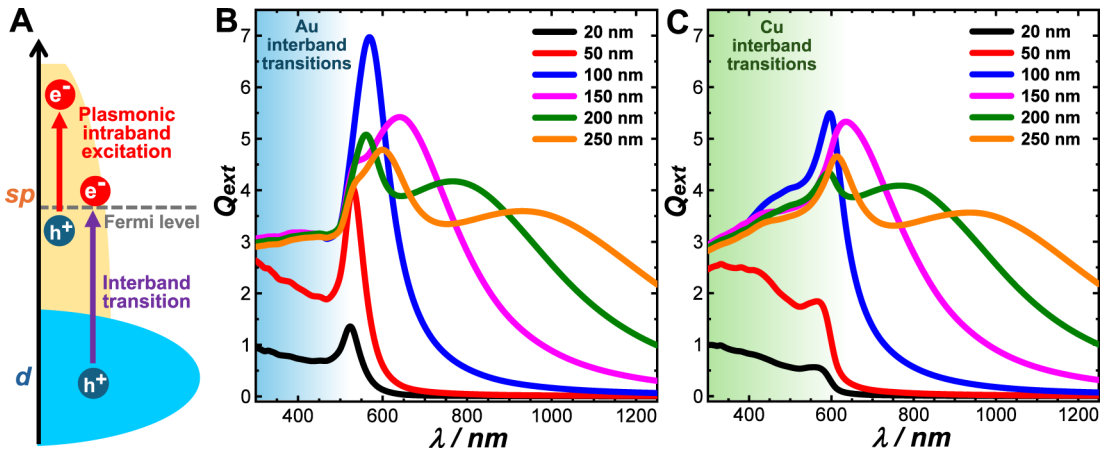

Figure 1. (A) Scheme illustrating the photoexcitations of interband and intraband hot carriers in a metal nanoparticle. (B) Calculated extinction efficiency, Q_{ext}, for (B) Au and (C) Cu nanospheres with various diameters surrounded by H_2O. The shaded regions correspond to the spectral windows in which interband transitions occur. In the Mie scattering theory calculations, the experimentally measured dielectric functions of Au and Cu reported by Johnson and Christy (ref 46) were used and the dielectric medium surrounding the nanospheres was set as water (refractive index of 1.33).

of interband hot carriers in metallic nanoparticles for photocatalysis remains relatively underexplored. Some recent studies suggest that interband hot carriers can be photocatalytically even more efficient than intraband hot carriers in driving certain types of reactions.[9,10,15−18] When plasmon resonances and interband transitions occur in well-separated spectral windows, the intraband and interband hot carriers can be selectively excited by choosing the appropriate excitation wavelengths. In certain materials, however, plasmon resonances may couple with interband transitions due to the spectral overlap of the two photoexcitation processes.[17,19] Consequently, interband damping of plasmon resonances becomes a prominent effect, significantly modifying the relative populations, energy distributions, and photocatalytic efficacies of intraband and interband hot carriers.

Bimetallic nanoparticles are structurally more tunable and functionally more versatile than their monometallic counterparts, creating ample room for further optimization of both light-matter and metal-adsorbate interactions.[20,21] A bimetallic materials system of particular interest to the plasmonic photocatalysis community has been antenna-reactor hybrid heteronanostructures,[22−29] in which a plasmonic metal, such as Au, Ag, Cu, and Al, functions as the light-harvesting and light-concentrating nanoantenna, while the reactor domains typically composed of Pt, Pd, Ru, or Ir serve as the catalytically active sites. The photocatalytic performances of these antenna-reactor nanohybrids can be fine-optimized either by tailoring the structures of the antenna and reactor domains independently or by tuning the antenna-reactor interactions without modifying the intrinsic features of each constituent.[22−29] Here, we focus on a fundamentally intriguing but less explored bimetallic photocatalyst system in which atoms of different metal elements are homogeneously intermixed to form single-phase alloy nanoparticles. These alloy nanoparticles may exhibit optical and photocatalytic properties strikingly different from those of their heterostructured counterparts.[20,30−32] The detailed structure-composition-property relationships underpinning the versatile photocatalytic behaviors of alloy nanoparticles in different optical excitation regimes remain elusive and worthy of in-depth investigations.

The alloy photocatalysts investigated in this work are composed of two coinage metal elements, Au and Cu. Monometallic nanoparticles made of Au and Cu exhibit interesting optical characteristics that are modulated by the spectral overlap of plasmon resonances with interband transitions in the visible region. While the resonant frequencies of plasmons can be finely tuned by varying the particle geometries and the local environments surrounding the nanoparticles, the energy threshold above which interband transitions occur is essentially determined by the energy gap between the edge of the *d* band and the Fermi level of the metal. The optical responses of Cu nanoparticles in the visible region are dominated by strong interband electronic transitions, which severely dampen the plasmon resonances in Cu.[33−36] In contrast to Cu, nanoparticles made of Au exhibit substantially stronger plasmonic characteristics in the visible region because of less spectral overlap between plasmon resonances and interband transitions in Au.[33−36] As demonstrated in this work, the degree of spectral overlap of plasmon resonances with interband transitions and the partition of intraband and interband excitations in Au−Cu alloy nanoparticles become highly tunable upon variation of either the particle sizes or the Cu/Au stoichiometric ratios. From the perspective of materials synthesis, Au and Cu also represent an ideal choice of elemental combination for binary alloy formation because Au and Cu atoms are thermodynamically miscible in the face-centered cubic (fcc) lattices over the entire stoichiometric range.[37−42] Precise control over the compositions and sizes of Au−Cu alloy nanoparticles can be experimentally achieved through deliberately designed multistep colloidal synthesis.[43,44] Built upon the success in composition- and size-controlled colloidal synthesis and detailed kinetic studies of a model photocatalytic reaction under deliberately controlled photoexcitation conditions, we have been able to elucidate how the variation of particle sizes and compositional stoichiometries modulates the photocatalytic efficacies of interband and intraband hot carriers in bimetallic Au−Cu alloy nanoparticles.

https://doi.org/10.1021/acsnanoscienceau.4c00035
ACS Nanosci. Au 2024, 4, 360−373

RESULTS AND DISCUSSIONS

Plasmon Resonances and Interband Transitions in Au and Cu Nanoparticles

The optical characteristics of Au and Cu are intimately tied to their intrinsic electronic band structures, which are featured by a diffuse conduction band comprising hybridized *s* and *p* states that span a broad energy range across the Fermi level and a narrower *d* band with a significantly higher density of states below the Fermi level[5] (see schematic illustration in Figure 1A). The energy gap between the *d* band edge and the Fermi level determines the onset for *d*-to-*sp* interband electronic transitions, which is ∼ 2.1 eV (∼590 nm) for Cu and ∼ 2.4 eV (∼516 nm) for Au,[33−36] respectively. Photoexcitation of the *d*-to-*sp* interband transitions results in highly energetic holes in the *d* band well below the Fermi level and excited electrons in the *sp* band near the Fermi level, respectively. In contrast, intraband hot carriers derived from plasmon decay exhibit drastically different energy distribution profiles, with hot electrons nonthermally distributed above the Fermi level, leaving holes below the Fermi level.

The plasmonic responses of a metallic nanoparticle are essentially dictated by the wavelength-dependent complex dielectric functions of the materials.[45] A plasmon can be resonantly excited at a wavelength where the real part of the dielectric function (ε') of a metal is negative, while the relative ε' values of the metal and the surrounding medium determine the plasmon resonance frequency. Because Au and Cu have very similar ε' values in the visible and near-infrared regions[46] (Figure S1A in the Supporting Information), Au and Cu nanoparticles of the same sizes, when dispersed in the same dielectric medium, are expected to have similar plasmon resonance frequencies, which was confirmed by the results of Mie theory calculations (Figure 1B,C). However, the optical efficiencies, which are defined as the ratios between optical and physical cross sections of the nanoparticles, can differ drastically between Au and Cu due to the damping of plasmon resonances, which is controlled by the imaginary part of the dielectric function (ε''). Cu has significantly higher ε'' than Au in the green part of the visible spectrum (500−570 nm)[46] due to stronger interband transitions in Cu (Figure S1B in the Supporting Information). As shown in previous publications,[47,48] seed-mediated colloidal syntheses of Au nanoparticles enabled precise tuning of the particle sizes in the range of ∼20−200 nm while well-preserving the quasi-spherical particle morphology, which resulted in an excellent match between the experimentally measured and the calculated extinction spectra. In the case of Cu nanoparticles, however, it remains challenging to rigorously compare the calculated and experimentally measured size-dependency of extinction spectra over such a broad size range primarily due to the intrinsic susceptibility of colloidal Cu nanoparticles against oxidation in the ambient environment[49] and the challenges in size-controlled synthesis of monodisperse Cu nanoparticles.[50]

Although the onsets for interband transitions in Au and Cu are spectrally fixed, the resonance frequencies of plasmons can be tuned simply by varying the nanoparticle sizes. In the sub-100 nm size regime, both Au and Cu nanoparticles exhibit a dipole plasmon resonance peak in the green part of the visible spectrum. The optical extinction efficiencies (Q_{ext}) of Cu nanoparticles at the plasmon resonance wavelengths are significantly weaker than those of Au nanoparticles primarily due to strong plasmon damping caused by interband transitions in Cu. As the particle size increases, the phase retardation effects become increasingly more pronounced, as reflected by the spectral redshift of the dipole plasmon resonances and the emergence of additional extinction peaks associated with higher-order multipole plasmon resonances (Figure 1B,C). When the particle size exceeds 150 nm, the dipole plasmons in both Au and Cu are resonantly excited below the onset of interband transitions. Benefiting from the spectral offset between plasmon resonances and interband transitions, the Q_{ext} values of Cu nanoparticles become comparable to those of Au nanoparticles at the resonant wavelengths of dipole plasmons. When the particle sizes are beyond 200 nm, Au and Cu nanoparticles exhibit essentially the same extinction spectral features below the onset of interband transitions due to minimal interband damping of plasmons. The optical extinction of Cu nanoparticles becomes particularly intense when various plasmon modes are resonant within a low-loss spectral window from 600 to 800 nm, where the ε'' values of Cu drop significantly and become comparable to those of Au. Both absorption and scattering by nanoparticles may contribute to the overall extinction of light, and the scattering-to-absorption ratios at specific wavelengths depend not only on the particle size but also on the nature of optical transitions (Figure S2 in the Supporting Information). In the small particle size regime below 50 nm, the extinction spectral features of Au and Cu nanoparticles are dominated by absorption with a negligible contribution from scattering. The scattering-to-absorption ratio increases with the particle size. When the particle size exceeds 150 nm, the light extinction caused by plasmon resonances becomes dominated by scattering in the spectral range below the onset of interband transitions. The light extinction originating from *d*-to-*sp* interband electronic transitions, however, remains essentially absorptive in nature regardless of the particle sizes for both Au and Cu.

Size- and Composition-Controlled Synthesis of Au−Cu Alloy Nanoparticles

The insights gained from monometallic Au and Cu nanoparticles laid a critical knowledge foundation for us to further develop a detailed understanding of the bimetallic Au−Cu alloy system. Colloidal Au−Cu alloy nanoparticles with carefully controlled particle sizes and Cu/Au stoichiometric ratios were synthesized through multistep nanocrystal growth and structure-transforming processes. We first adopted a seed-mediated growth method[51] to synthesize colloidal Au nanoparticles with a quasi-spherical morphology and tunable average sizes in the range of 50−200 nm (Figure S3 in the Supporting Information). The Au nanoparticles were then utilized as the seeds to grow Au@Cu_2O core−shell nanoparticles with precisely controlled core and shell dimensions following a previously reported protocol.[52] Colloidal Au@Cu_2O core−shell nanoparticles suspended in tetraethylene glycol were then fully converted into Au−Cu alloy nanoparticles after being maintained at 300 °C for 1 h.[43,44] Previously reported structural characterizations using scanning electron microscopy (SEM), transmission electron microscopy (TEM), powder X-ray diffraction (PXRD), and energy dispersive spectroscopy (EDS)-based elemental mapping revealed that the Au and Cu atoms were fully intermixed to form homogeneous solid solutions in these nanoparticles rather than forming locally segregated monometallic domains.[44] The overall particle sizes and Cu/Au atomic ratios

https://doi.org/10.1021/acsnanoscienceau.4c00035
ACS Nanosci. Au 2024, 4, 360−373

of the resulting alloy nanoparticles could be systematically tuned by varying the core and shell dimensions of the parental Au@Cu_2O core−shell nanoparticles. Using this versatile synthetic approach, we were able to tune the Cu/Au stoichiometric ratios in alloy nanoparticles with precisely controlled sizes in the range of ∼ 50−200 nm. When using this method for synthesizing smaller alloy nanoparticles in the sub-50 nm size regime, we ran into some challenging issues associated with phase segregation and the formation of intermetallic phases, which deserve further investigation. For the comparative studies presented in this work, we synthesized a group of Au−Cu alloy nanoparticle samples that exhibited tunable average particle sizes in the range of ∼50−200 nm but possessed nominally the same Cu/Au compositional stoichiometries around 4.2 (Figure S4 in the Supporting Information). We also synthesized another group of Au−Cu alloy nanoparticles with similar sizes around 140 nm but different Cu/Au stoichiometric ratios (Figure S5 in the Supporting Information) for comparison. In all cases, the Cu and Au atoms in nanoparticles were homogeneously intermixed to form single fcc phase solid solutions without any detectable phase-segregated monometallic domains or ordered intermetallic phases in the PXRD patterns (Figures S4A and S5A in the Supporting Information). The nanoparticle sizes were analyzed on the basis of TEM images, and the distributions of particle sizes were shown as histograms in Figures S3E, S4F, and S5F in the Supporting Information. The Cu/Au stoichiometric ratios were quantified either through EDS-based elemental analysis (Figure S6 in the Supporting Information) or by analyzing the PXRD results (Figures S4A and S5A in the Supporting Information) using Vegard's law,[53] a heuristic approach assuming the lattice parameters of a binary alloy as the weighted means of the two constituents. Because the Au−Cu alloy system only deviated slightly from the ideal situation described by Vegard's law,[54] the Cu/Au stoichiometric ratios calculated from PXRD agreed with the EDS results very well. We labeled each alloy nanoparticle sample as $AuCu_x$-Y, in which x and Y refer to the stoichiometric ratio of Cu/Au (quantified by EDS) and the average particle diameter (in the units of nm), respectively. The sample labels, particle sizes (measured by TEM), and compositional stoichiometries (quantified by EDS and PXRD) of various monometallic Au and Au−Cu alloy nanoparticles investigated in this work are listed in Table 1.

Table 1. Sizes and Compositions of Monometallic Au and Bimetallic Au−Cu Alloy Nanoparticle Samples Investigated in This Work

	Cu/Au atomic ratios			
	PXRD	EDS	particle size/nm	sample label
Au-i	0	0	58 ± 7	Au-58
Au-ii	0	0	139 ± 12	Au-139
Au-iii	0	0	180 ± 13	Au-180
AuCu-i	4.5	4.3 ± 0.3	58 ± 6	$AuCu_{4.3}$-58
AuCu-ii	4.3	4.4 ± 0.4	115 ± 11	$AuCu_{4.4}$-115
AuCu-iii	4.5	4.2 ± 0.3	142 ± 12	$AuCu_{4.2}$-142
AuCu-iv	4.7	4.5 ± 0.3	178 ± 15	$AuCu_{4.5}$-178
AuCu-v	2.0	2.2 ± 0.2	138 ± 11	$AuCu_{2.2}$-138
AuCu-vi	0.72	0.83 ± 0.07	140 ± 11	$AuCu_{0.83}$-140
AuCu-vii	0.23	0.27 ± 0.03	141 ± 13	$AuCu_{0.27}$-141

Size- and Composition-Dependent Photocatalytic Behaviors of Au−Cu Alloy Nanoparticles

Precise control over the particle sizes and alloy compositions enabled us to systematically investigate the size- and composition-dependent photocatalytic behaviors of Au−Cu alloy nanoparticles under intra- and interband photoexcitation conditions. The model reaction we chose for the detailed kinetic studies was the photocatalytic degradation of Rhodamine B (RhB), a toxic xanthene dye commonly found in textile wastewater. The photocatalytic reactions occurred in an aqueous medium under ambient air, with colloidal Au or Au−Cu alloy nanoparticles (∼ 1.0×10^9 particles mL^{-1}) serving as the photocatalysts and H_2O_2 serving as an electron acceptor, respectively. The initial concentrations of RhB and H_2O_2 were 2 μM and 2 mM, respectively, and the total volume of the reactant-catalyst mixtures was 2.0 mL. Collimated continuous wave (cw) diode lasers with emission wavelengths at 445, 520, 638, 785, and 980 nm were used as the excitation sources. As schematically illustrated in Figure 2A, the plasmon-derived energetic hot electrons distributed above the Fermi level (−5.1 eV vs vacuum for Au, −4.7 eV vs vacuum for Cu,[33,55] and between −5.1 and −4.7 eV vs vacuum for Au−Cu alloys) could get injected into H_2O_2 to trigger the cleavage of O−O bond, which led to the formation of $OH^{\bullet}$ radicals, a reactive oxygen species (ROS) causing the degradation of RhB into fully mineralized small molecules, such as CO_2 and H_2O.[56,57] The plasmonic hot holes below the Fermi level were most likely utilized to drive the O_2 evolution from H_2O (standard reduction potential of O_2/H_2O: −5.7 eV vs vacuum[58]). Upon photoexcitation of the *d*-to-*sp* interband excitations, both the hot electrons and holes became exploitable for the photocatalytic degradation of RhB. The energetic interband hot holes in the *d* band well below the Fermi level were capable of oxidizing H_2O to produce $OH^{\bullet}$ radicals (standard reduction potential of $OH^{\bullet}/H_2O$: −7.3 eV vs vacuum[59]), while the excited electrons in the *sp* band could effectively reduce H_2O_2 into $OH^{\bullet}$ because the lowest unoccupied molecular orbital (LUMO) of H_2O_2, which was antibonding in nature, was closely aligned with the Fermi level.[60−62] The progress of photocatalytic RhB degradation could be monitored based on the intensity evolution of the characteristic peak of RhB centered at 553 nm in the UV−visible absorption spectra (Figure 2B). Within the RhB concentration range investigated in this work, the absorbance at 553 nm (A) was directly proportional to the concentration of RhB (C) according to Beer−Lambert's Law. It is noteworthy that through UV−visible absorption spectroscopic measurements, we essentially monitored the decolorization of RhB rather than all elementary steps involved in the mechanistically complicated, multistep photodegradation process. The apparent reaction kinetics under our experimental conditions (H_2O_2 was in large excess with respect to RhB) could be well-described by a simple pseudo-first-order rate law:

$$-\ln\left(\frac{A}{A_0}\right) = -\ln\left(\frac{C}{C_0}\right) = kt \quad (1)$$

where k is the apparent first-order rate constant, t is reaction time, C_0 is the initial concentration of RhB (2 μM), and A_0 is initial absorbance at 553 nm. Taking the reactions catalyzed by $AuCu_{4.5}$-178 as an example, the dark reaction was observed to be kinetically sluggish without any detectable progress over several hours, whereas photoexcitation of interband transitions

https://doi.org/10.1021/acsnanoscienceau.4c00035
ACS Nanosci. Au 2024, 4, 360−373

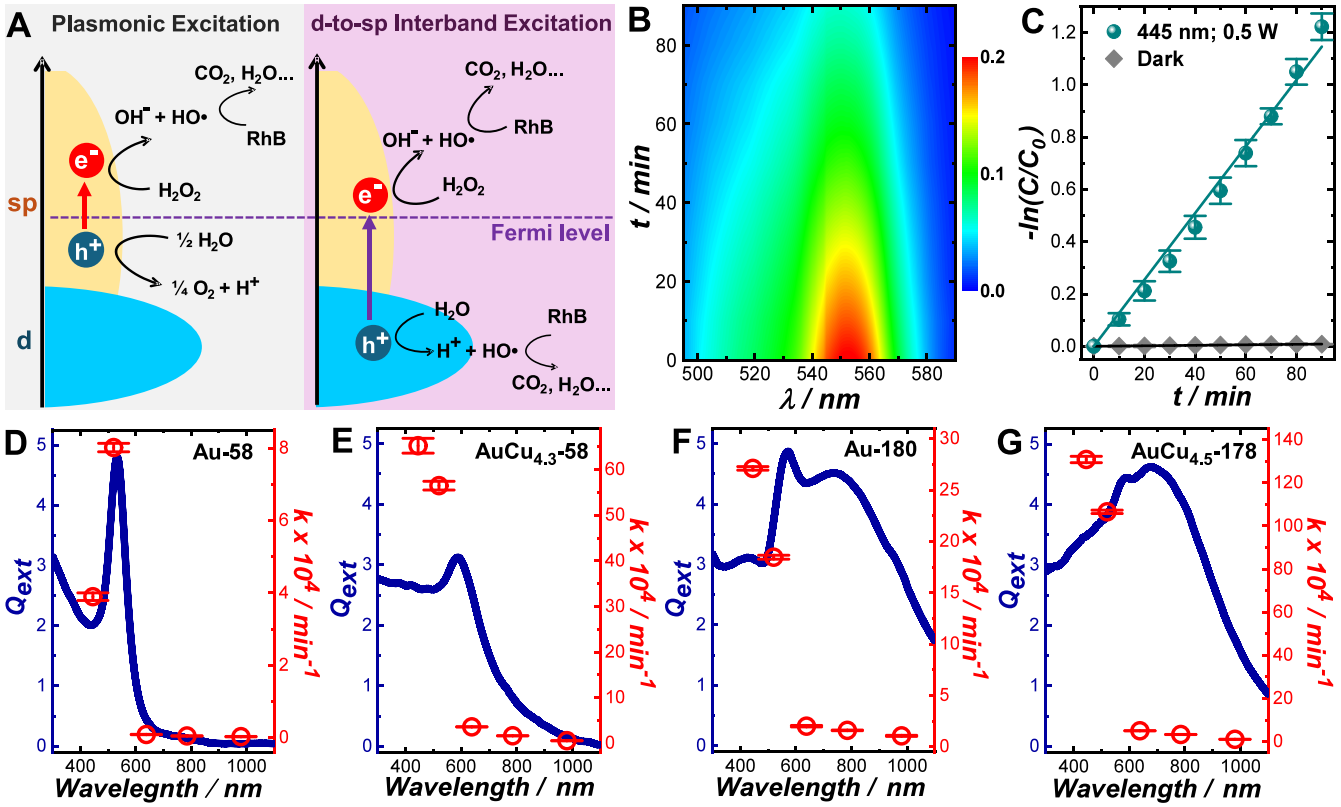

Figure 2. (A) Schematic illustration of photocatalytic degradation of RhB using H_2O_2 as an electron acceptor driven by (left panel) plasmonic intraband and (right panel) interband hot carriers. (B) Temporally evolving UV−vis absorption spectra showing the kinetics of RhB degradation catalyzed by $AuCu_{4.5}$-178 at λ_{ex} of 445 nm and P_{ex} of 0.5 W. The color scale shows the absorbance of RhB in the solution phase. (C) Temporal evolution of $-\ln(C/C_0)$ in the dark and under continuous laser illumination (λ_{ex} of 445 nm and P_{ex} of 0.5 W). The error bars represented the standard deviations of three experimental runs under each reaction condition. The solid lines showed the least-squares curve fitting results. Experimentally measured extinction spectra of various Au and Au−Cu alloy nanoparticle samples and the apparent rate constants of photocatalytic RhB degradation at various λ_{ex}s: (D) Au-58, (E) $AuCu_{4.3}$-58, (F) Au-180, and (G) $AuCu_{4.5}$-178. The reaction kinetics were measured at 5 different λ_{ex}s (445, 520, 638, 785, and 980 nm) and a fixed P_{ex} of 0.5 W. The concentration of colloidal nanoparticles in the reactant-catalyst mixtures was kept at 1×10^9 particles mL^{-1}. The error bars represented the standard deviations of the least-squares curve fitting.

at an excitation wavelength (λ_{ex}) of 445 nm drastically accelerated the degradation reactions (Figure 2C). In the absence of any colloidal photocatalysts, slow RhB degradation caused by H_2O_2 photolysis was observed under blue laser illumination (λ_{ex} of 445 nm), whereas laser illumination at longer λ_{ex}s did not lead to any detectable degradation of RhB (Figure S7 in the Supporting Information). To accurately analyze the kinetic results of photocatalytic reactions, the contribution of H_2O_2 photolysis at λ_{ex} = 445 nm was subtracted from the overall reaction rates. Through least-squares curve fitting using the first-order rate law, we were able to extract the values of k from the experimentally measured kinetic results and systematically compare the k values for different photocatalyst materials under a broad range of light illumination conditions.

We chose monometallic Au and bimetallic Au−Cu alloy nanoparticles in two different particle size regimes within and beyond the quasi-static limit for detailed comparative investigations. We studied the kinetics of the reactions catalyzed by Au-58, $AuCu_{4.3}$-58, Au-180, and $AuCu_{4.5}$-178 under continuous laser illumination at a fixed excitation power (P_{ex}) of 0.5 W but different λ_{ex}s (445, 520, 638, 785, and 980 nm). The detailed kinetic results are shown in Figure S8 in the Supporting Information. To facilitate heat dissipation and eliminate the effects of photothermal heating, the catalyst−reactant mixtures were immersed in a water bath (4 L in volume) under constant magnetic stirring (200 rpm). Under our experimental conditions, the temperature in the solution phase was only elevated by less than 3 °C under continuous laser illumination at various λ_{ex}s (Figure S9 in the Supporting Information), suggesting that the photocatalytic RhB degradation was primarily driven by photoexcited hot carriers rather than being triggered by photothermal heating. Although monometallic Cu nanoparticles were highly susceptible to oxidation when exposed to air[63] or H_2O_2,[64] alloying Cu with Au significantly increased the chemical stability of metallic Cu.[40,44] Despite its Cu-rich composition, $AuCu_{4.5}$-178 exhibited excellent photocatalytic durability and structural stability over multiple cycles of reactions. As shown in Figure S10 in the Supporting Information, the photocatalytic activity of $AuCu_{4.5}$-178 was well-preserved over three cycles of reactions. The recycled $AuCu_{4.5}$-178 photocatalysts exhibited almost no dimensional or morphological changes in the TEM images, and the Au:Cu stoichiometric ratios remained essentially unchanged during multiple reaction cycles, as revealed by PRXD and EDS results (Figure S11 in the Supporting Information).

We first compared Au-58 and $AuCu_{4.3}$-58, both of which had a relatively small average particle size of 58 nm, well within the quasi-static limit. Their extinction spectral features were

https://doi.org/10.1021/acsnanoscienceau.4c00035
ACS Nanosci. Au 2024, 4, 360−373

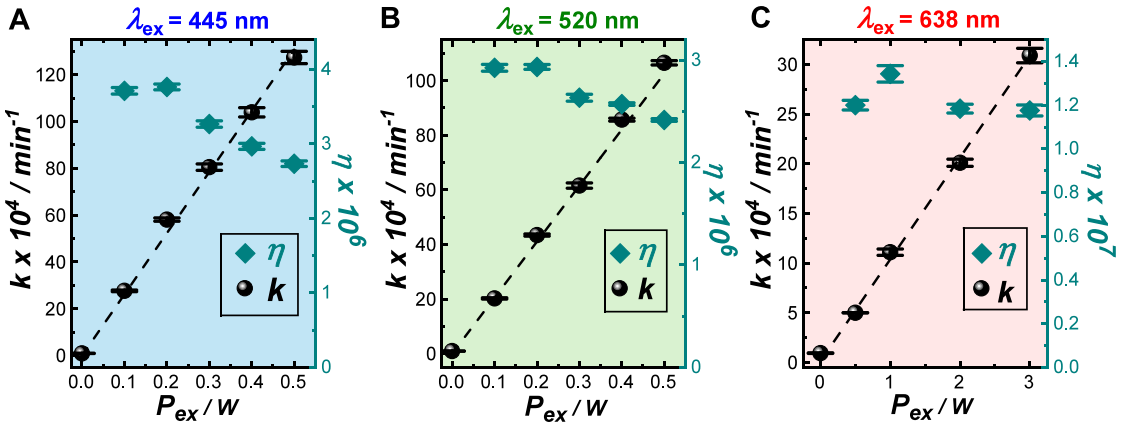

Figure 3. P_{ex}-dependence of k and η of $AuCu_{4.5}$-178 at λ_{ex}s of (A) 445, (B) 520, and (C) 638 nm. In all cases, the concentration of nanoparticles in the reactant-catalyst mixtures was kept at 1×10^9 particles mL^{-1}.

dominated by light absorption caused by the dipole plasmon resonances and *d*-to-*sp* interband electronic transitions. For direct comparison, we plotted the photocatalytic action spectra (λ_{ex}-dependence of k) on top of the extinction spectra (λ_{ex}-dependence of Q_{ext}) in Figure 2D,E. In the case of Au-58, the action spectrum matched the extinction spectrum very well (Figure 2D). Au-58 was observed to be photocatalytically active when exciting the dipole plasmon resonance at 520 nm and the *d*-to-*sp* interband transitions at 445 nm, respectively. Under off-resonant conditions at longer λ_{ex}s (638, 785, and 980 nm), Au-58 became essentially inactive toward the RhB degradation reactions. The HOMO-to-LUMO electronic excitations in RhB molecules in an aqueous solution resulted in a characteristic light absorption band centered at 553 nm (Figure S12A in the Supporting Information). At λ_{ex}s of 445, 638, 785, and 980 nm, the excitation lasers were completely off-resonant with the electronic transitions in RhB. At the λ_{ex} of 520 nm, which overlapped with the shoulder of the absorption band, electronic transitions in RhB could still be photoexcited. Although intramolecular electronic excitations in certain adsorbates may lead to photocatalytic reactions,[65−68] we did not observe any photodegradation when illuminating an aqueous solution of RhB by the 520 nm laser (Figure S12B in the Supporting Information). The introduction of Au-58 catalysts into the RhB solution resulted in a negligible enhancement in photodegradation, indicating that the plasmon-enhanced intramolecular excitation played a rather insignificant role in triggering the photodegradation of RhB under our experimental conditions. Only when H_2O_2 was added as the hot electron acceptors could Au-58 function as efficient photocatalysts for $OH^{\bullet}$ generation and RhB degradation at the λ_{ex} of 520 nm, further verifying the hot electron-driven reaction mechanism.

In contrast to Au-58, $AuCu_{4.3}$-58 exhibited a photocatalytic action spectrum that deviated significantly from its extinction spectral profile (Figure 2E). In the spectral range above the onset of interband transitions, the values of k were more than 1 order of magnitude higher than those below the interband transition onset, strongly suggesting that the interband hot carriers were photocatalytically more efficient than the intraband hot carriers. With the particle size fixed at 58 nm, alloying Au with Cu led to a downshift of the onset for interband transitions, resulting in interband damping of the visible plasmon resonance and a more than 7-fold increase in k at λ_{ex} of 520 nm. For the reactions driven by interband hot carriers at a λ_{ex} of 445 nm, the reaction catalyzed by $AuCu_{4.3}$-58 appeared more than 10 times faster than that catalyzed by Au-58. All these observations coherently suggested that in the small particle size regime where the extinction was dominated by absorption, the photocatalytic efficacies of interbond hot carriers could be drastically enhanced by alloying Au with Cu. In addition, the interband hot carriers in Au−Cu alloy nanoparticles could be more efficiently harnessed for photocatalysis than their counterparts derived from intraband plasmonic excitations. In the presence of *tert*-butyl alcohol (TBA), which was an efficient $OH^{\bullet}$ scavenger, the photodegradation of RhB over Au-58 and $AuCu_{4.3}$-58 was effectively suppressed at the λ_{ex} of 520 nm, verifying that $OH^{\bullet}$ was responsible for the RhB photodegradation (Figure S13 in the Supporting Information).

We also studied the photocatalytic behaviors of Au-180 and $AuCu_{4.5}$-178, both of which were in size regimes beyond the quasi-static limit. The emergence of higher-order multipolar plasmon resonances was clearly observed in the extinction spectra (Figure 2F,G). Upon an increase of particle size from ∼58 to ∼178 nm, the reaction rate at λ_{ex} of 520 nm exhibited a 2.2-fold enhancement in the monometallic Au nanoparticles and a 1.9-fold enhancement in the Cu-rich alloy nanoparticles, respectively, indicating that the number of hot carriers exploitable for RhB degradation in each nanoparticle increased with the particle size. At λ_{ex} of 445 nm, the reaction rate increased by almost 7 times in the Au nanoparticles and 5 times in the Cu-rich alloy nanoparticles, respectively, when the particle size increased from ∼58 to ∼178 nm. On both Au-180 and $AuCu_{4.5}$-178, the reaction rates at λ_{ex} of 445 nm became higher than at λ_{ex} of 520 nm, because shorter excitation wavelengths resulted in the creation of deeper and more energetic holes in the *d* band. On the other hand, larger nanoparticles exhibited higher light scattering cross sections in comparison to their smaller counterparts. At λ_{ex} of 445 nm, the elastically scattered photons from larger nanoparticles might trigger the photolysis of H_2O_2, which could provide an additional contribution to the kinetic enhancement of RhB degradation. For both Au-180 and $AuCu_{4.5}$-178, plasmonic intraband excitations at λ_{ex}s of 638 and 785 nm were photocatalytically much less efficient than the interband excitations (Figure 2F,G), because these nanoparticles beyond the quasi-static limit behaved as strong light scatterers rather than absorbers at their plasmon resonance frequencies[45] and thus became less efficient in producing hot carriers through

https://doi.org/10.1021/acsnanoscienceau.4c00035
ACS Nanosci. Au 2024, 4, 360−373

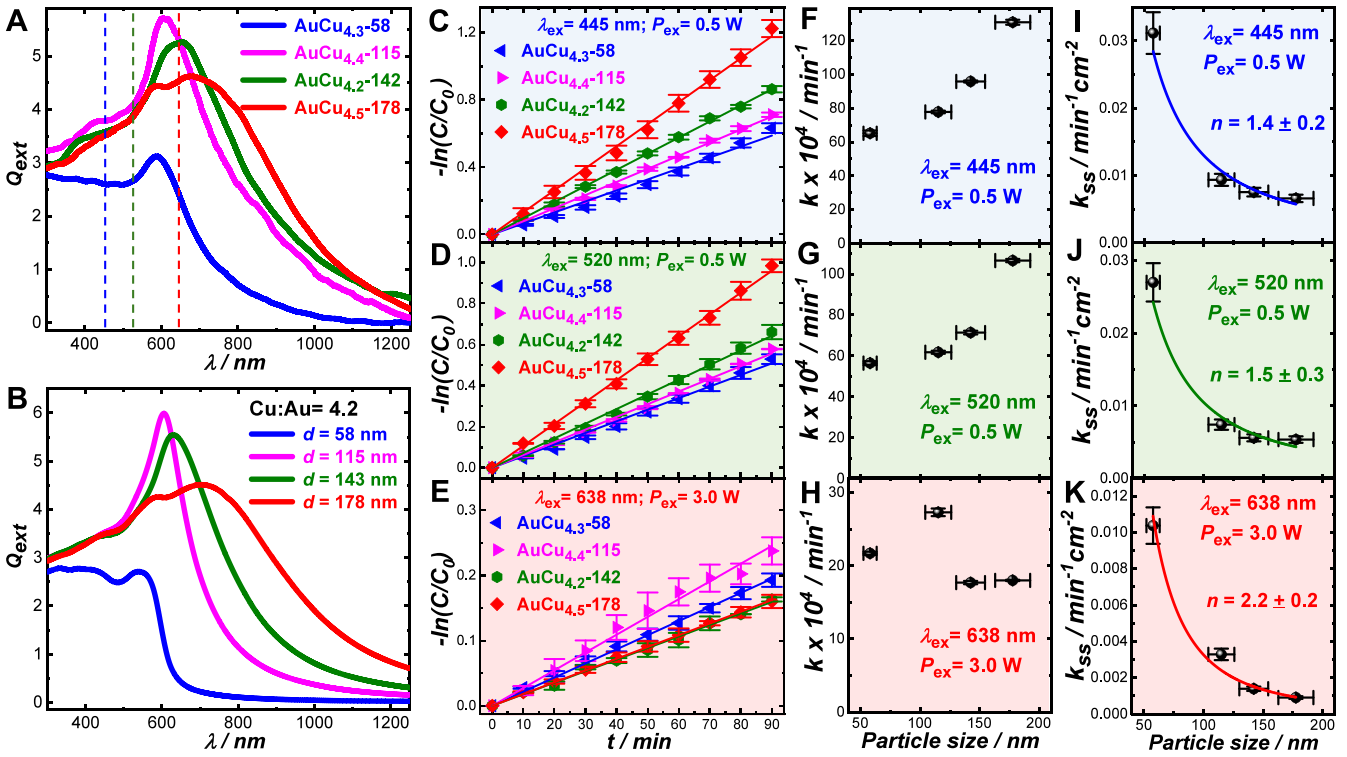

Figure 4. (A) Experimentally measured extinction spectra of Au−Cu alloy nanoparticles with various sizes and a nominally fixed Cu/Au stoichiometric ratio of around 4.2. The vertical dash lines indicate the wavelengths of excitation lasers used for photocatalysis. (B) Calculated extinction spectra of a spherical Au−Cu alloy nanoparticle with a Cu/Au stoichiometric ratio of 4.2 and varying diameter of 58, 115, 142, and 178 nm. The dielectric medium surrounding the nanoparticles was water. Temporal evolution of $-\ln(C/C_0)$ during photocatalytic degradation of RhB at (C) λ_{ex} of 445 nm and P_{ex} of 0.5 W, (D) λ_{ex} of 520 nm and P_{ex} of 0.5 W, and (E) λ_{ex} of 638 nm and P_{ex} of 3.0 W. Plots of k as a function of particle diameters at (F) λ_{ex} of 445 nm and P_{ex} of 0.5 W, (G) λ_{ex} of 520 nm and P_{ex} of 0.5 W, and (H) λ_{ex} of 638 nm and P_{ex} of 3.0 W. Size dependence of surface specific rate constants, k_{ss} (k normalized against surface area of nanoparticles), of Au−Cu alloy nanoparticles (Cu/Au ratios around 4.2) at (I) λ_{ex} of 445 nm and P_{ex} of 0.5 W, (J) λ_{ex} of 520 nm and P_{ex} of 0.5 W, and (K) λ_{ex} of 638 nm and P_{ex} of 3.0 W. The curve fitting results are shown as solid curves.

Landau damping than their smaller counterparts within the quasi-static limit.

To gain further mechanistic insights, we investigated the P_{ex} dependency of the rate of $AuCu_{4.5}$-178-catalyzed reactions under interband (λ_{ex} = 445 and 520 nm) and plasmonic intraband excitations (λ_{ex} = 638 nm). The detailed kinetic results are shown in Figure S14 in the Supporting Information. The rate constant appeared directly proportional to P_{ex} at all λ_{ex}s within the P_{ex} range we investigated (Figure 3). Such a linear dependence of k on P_{ex} indicated that the degradation of RhB was primarily driven by photoexcited hot carriers rather than being triggered by photothermal heating (Arrhenius-type P_{ex} dependence of k),[3,69−73] which was in line with the limited temperature elevation observed during the reactions (Figure S9 in the Supporting Information). Under our photoexcitation conditions (cw illumination with relatively low photon flux densities), we did not observe any apparent superlinearity in the P_{ex}-dependence of k that could possibly arise from multiphoton absorption processes.[3,69,72,74]

On the basis of the λ_{ex}- and P_{ex}-dependent kinetic results, we further calculated the apparent quantum efficiency, η, using the following equation:

$$\eta = \frac{hcVN_A(C_0 - C_{1h})}{P_{ex}\lambda_{ex} \times 3600s} \quad (2)$$

where h is the Planck's constant (6.626×10^{-34} m^2 kg s^{-1}), c is the speed of light (3.0×10^8 m s^{-1}), C_0 is the initial concentration of RhB (2×10^{-6} M), C_{1h} is the concentration of RhB in the solution after a reaction time of 1 h, V is the volume of the solution (2.0×10^{-3} L), and N_A is the Avogadro's number (6.022×10^{23} mol^{-1}). When calculating the η values, we assumed that one hot carrier was utilized to induce the decolorization of each RhB molecule. However, the η values calculated in this work significantly underestimated the quantum efficiencies because the complete degradation of one RhB molecule involved the participation of multiple hot carriers.[56,57] The η values of the interband hot carrier-driven reactions at λ_{ex}s of 445 (Figure 3A) and 520 nm (Figure 3B) decreased when P_{ex} increased. A higher photon flux gave rise to a more rapid generation of photoexcited hot carriers in the nanoparticles, leading to faster consumption of the reactant molecules. For a pseudo-first-order reaction, the reaction rates decreased as the reaction proceeded. Within a fixed reaction time, increasing the excitation power resulted in decreased apparent quantum yields.[75] Because the intraband hot carrier-driven reactions were much slower than the interband hot carrier-driven reactions at a fixed excitation power, η became less sensitively dependent upon P_{ex}. Therefore, η was observed to be almost P_{ex}-independent in the P_{ex} range of 0−3 W in the case of intraband hot carrier-driven reactions at an λ_{ex} of 638 nm (Figure 3C). The η values at λ_{ex}s of 445 and 520 nm were on the order of 10^{-6}, more than 10 times higher than those achievable at λ_{ex} of 638 nm, indicating that direct photoexcitation of d-to-sp interband transitions in Au−Cu alloy

https://doi.org/10.1021/acsnanoscienceau.4c00035
ACS Nanosci. Au 2024, 4, 360−373

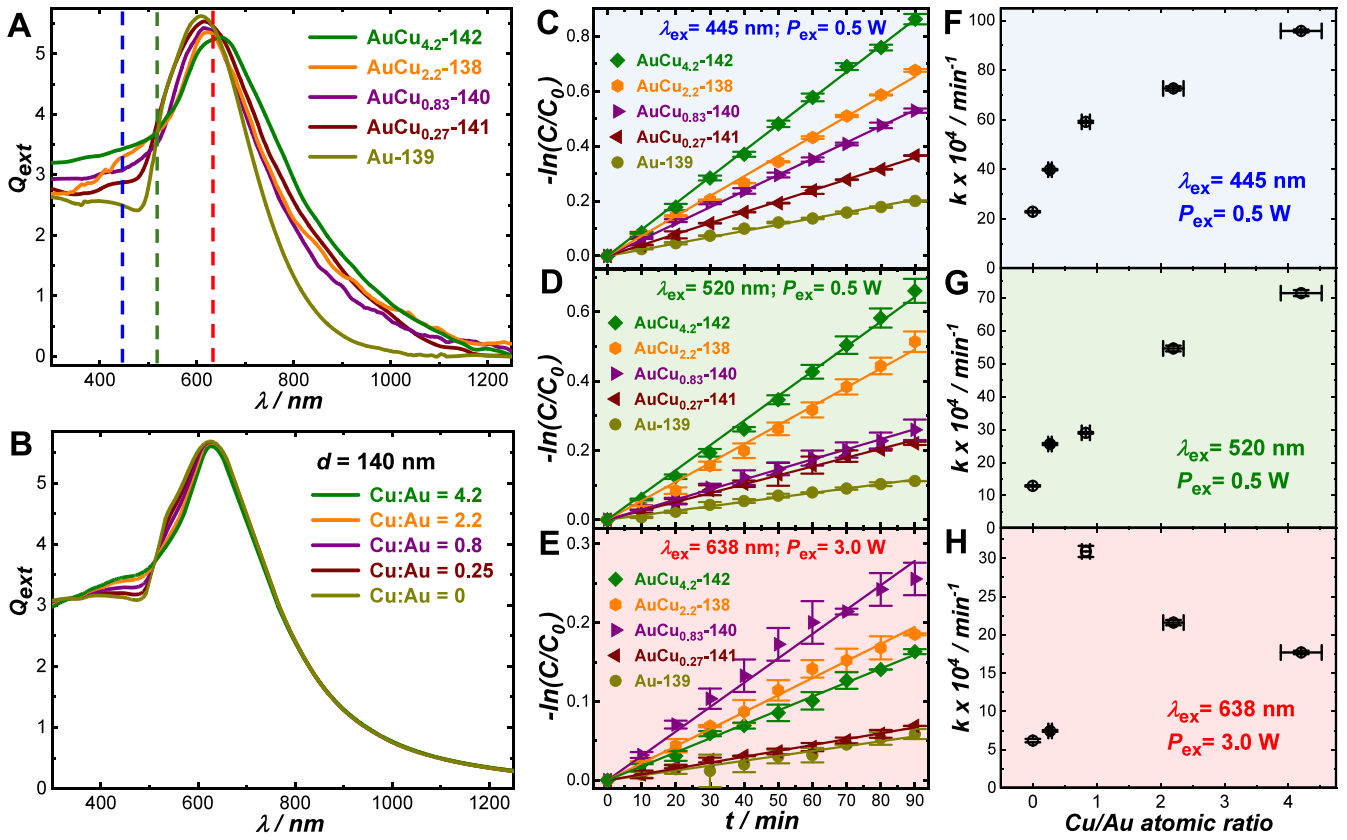

Figure 5. (A) Experimentally measured extinction spectra of Au−Cu alloy nanoparticles with various Cu/Au stoichiometric ratios and monometallic Au nanoparticles, all of which were around 140 nm in diameter. The vertical dash lines indicate the wavelengths of excitation lasers used for photocatalysis. (B) Calculated extinction spectra of a spherical Au−Cu alloy nanoparticle that was 140 nm in diameter with varying Cu/Au atomic ratio of 4.2, 2.2, 0.8, 0.25, and 0. The dielectric medium surrounding the nanoparticles was water. Temporal evolution of $-\ln(C/C_0)$ during photocatalytic degradation of RhB at (C) λ_{ex} of 445 nm and P_{ex} of 0.5 W, (D) λ_{ex} of 520 nm and P_{ex} of 0.5 W, and (E) λ_{ex} of 638 nm and P_{ex} of 3.0 W. Plots of k as a function of Cu/Au atomic ratio at (F) λ_{ex} of 445 nm and P_{ex} of 0.5 W, (G) λ_{ex} of 520 nm and P_{ex} of 0.5 W, and (H) λ_{ex} of 638 nm and P_{ex} of 3.0 W.

nanoparticles was more efficient in producing hot carriers exploitable for photocatalytic RhB degradation than the plasmonic intraband excitations.

To investigate the size-dependent photocatalytic behaviors of Au−Cu alloy nanoparticles in greater detail, we systematically compared the rates of the reactions catalyzed by $AuCu_{4.3}$-58, $AuCu_{4.4}$-115, $AuCu_{4.2}$-142, and $AuCu_{4.5}$-178, which represented a set of Cu-rich alloy nanoparticles with nominally the same Cu/Au stoichiometries but different particle sizes across the quasi-static limit. As the average particle size increased, the dipole plasmon resonance progressively red-shifted to longer wavelengths, and higher-order multipole plasmonic features emerged in the extinction spectra (Figure 4A). All of the experimentally observed size-dependent extinction spectral features were well-reproduced by discrete dipole approximation (DDA) calculations (Figure 4B). Through DDA calculations, the overall extinction spectra could be further decomposed into absorption and scattering spectra separately (Figure S15 in the Supporting Information). The interband transitions in the alloy nanoparticles were photoexcited at λ_{ex}s of 445 and 520 nm at a P_{ex} of 0.5 W, while the plasmon resonances were excited at λ_{ex} of 638 nm at a P_{ex} of 3.0 W. The detailed kinetic results under various photoexcitation conditions are shown in Figure 4C−E. Under optical excitation of interband transitions, k was observed to increase monotonically with the particle size (Figure 4F,G). On one hand, larger nanoparticles had higher light-absorption cross sections for interband excitations and were able to produce more interband hot carriers in each particle. On the other hand, the photocatalytic enhancement might also get compromised by increased light scattering from larger nanoparticles in the wavelength range for interband transitions (Figure S15 in the Supporting Information). Under plasmonic intraband excitations, however, we did not observe any clear trend in the size-dependency of k (Figure 4H) because the efficiency of photogeneration of intraband hot carriers was not only determined by the frequency match between the plasmon resonances and the excitation photons but also modulated by the relative contributions of absorption vs scattering at the plasmon resonance frequencies. Although the Au−Cu alloy nanoparticles were purified through centrifugation multiple times before they were used for photocatalysis, residual capping ligands, polyvinylpyrrolidone (PVP) in our case, might still be present on the nanoparticle surfaces. It was previously reported that surface-adsorbed PVP mediated the plasmon-driven anisotropic growth of Au nanoprisms by serving as a photochemical relay for interfacial hot electron transfer.[76] At this stage, we did not see any evidence showing that the residual PVP on nanoparticle surfaces played any significant active roles in the photocatalytic degradation of RhB. Since all of the alloy nanoparticle samples were synthesized using PVP as the capping ligands, the

https://doi.org/10.1021/acsnanoscienceau.4c00035
ACS Nanosci. Au 2024, 4, 360−373

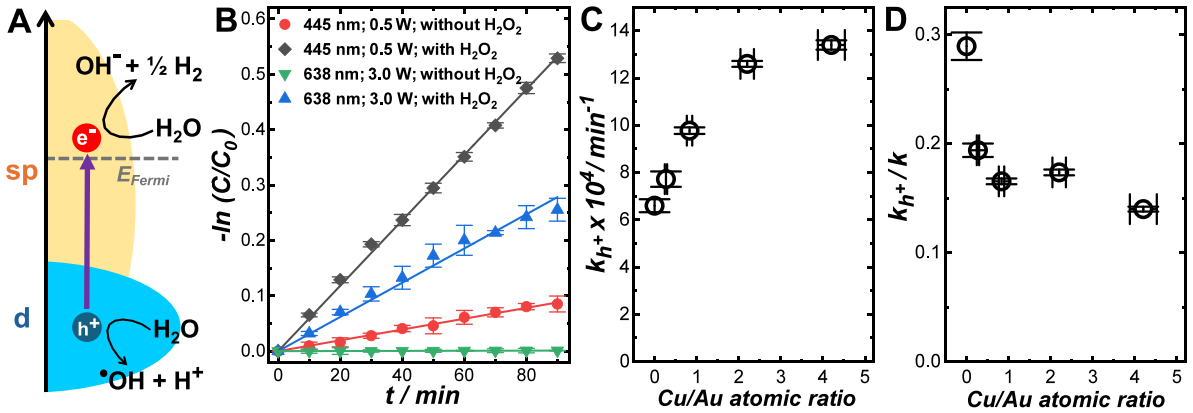

Figure 6. (A) Schematic illustration of interband hot hole-driven photocatalysis in the absence of H_2O_2. (B) Temporal evolution of $-\ln(C/C_0)$ during photocatalytic degradation of RhB catalyzed by $AuCu_{0.83}$-140 at λ_{ex}s of 445 nm (P_{ex} of 0.5 W) and 638 nm (P_{ex} of 3.0 W) in the presence and absence of H_2O_2. Alloy composition-dependence of (C) the hot hole-driven reaction rate constant, k_{h+}, and (D) the ratios between k_{h+} and k for reactions catalyzed by Au and Au−Cu alloy nanoparticles with average diameters around 140 nm.

differences in photocatalytic behaviors observed among various nanoparticle samples at different excitation wavelengths were unlikely to be caused by the presence of PVP.

We further calculated the surface-specific rate constants, k_{ss}, by normalizing the values of k against the nanoparticle surface areas, which reflected the relative abundance of hot carriers at the nanoparticle surfaces. As shown in Figure 4I−K, the k_{ss} values under interband excitations were approximately 1 order of magnitude higher than those under plasmonic intraband excitations, suggesting that the surface densities of interband hot carriers were significantly higher than those of intraband hot carriers. We also observed that k_{ss} decreased upon an increase in the particle size, regardless of whether the reactions were driven by interband or intraband hot carriers. Because the relaxation and thermalization of hot carriers might start immediately after photoexcitation before the hot carriers reached the nanoparticle surfaces and got transferred to molecular adsorbates, the hot carrier diffusion inside the nanoparticles became a critical factor limiting the surface abundance and utilization efficiencies of hot carriers for photocatalysis.[77] The size-dependence of k_{ss} was fitted with the following empirical equation:

$$k_{ss} = \frac{B}{\left(\frac{d}{1nm}\right)^n} \quad (3)$$

where d is the diameter of the alloy nanoparticles, n is an exponent, and B is a fractional coefficient corresponding to the k_{ss} value at d of 1 nm. Upon increase of particle size, the k_{ss} under plasmonic intraband excitations at λ_{ex} of 638 nm (n = 2.2 ± 0.2) decayed more rapidly than those under interband excitations (n = 1.4 ± 0.2 at λ_{ex} of 445 nm; n = 1.5 ± 0.3 at λ_{ex} of 520 nm). The hot carriers generated *via* interband excitations and Landau damping had different energy distribution ranges above/below the metal's Fermi level and therefore might have different lifetimes and diffusion lengths. If the observed photocatalytic activity was solely determined by the diffusion of hot carriers across the nanoparticle matrices, then the value of n should be expected to be 1.[77] The significantly higher values of n observed in our case strongly suggested that the nanoparticle sizes were significantly larger than the characteristic diffusion lengths of the hot carriers, and the carrier diffusion might be further complicated by other processes, such as electron−electron, electron−defect, and electron−phonon scattering.

To gain further insights into the composition-dependence of photocatalytic activities, we systematically compared the photocatalytic efficacies of $AuCu_{4.2}$-142, $AuCu_{2.2}$-138, $AuCu_{0.83}$-140, $AuCu_{0.27}$-141, and Au-139, a set of nanoparticle samples with the same average particle sizes around 140 nm but different Cu/Au stoichiometric ratios. We did not include monometallic Cu nanoparticles for comparison because of the poor chemical stability of Cu nanoparticles in an aqueous environment under ambient air and the challenges in the size-controlled synthesis of monodisperse Cu nanoparticles with a uniform quasi-spherical morphology. In this relatively large size regime beyond the quasi-static limit, the dipole plasmon resonances were red-shifted into the spectral region below the onset of interband transitions. The resonant frequencies of plasmons and the Q_{ext} values at the plasmon resonance frequencies appeared essentially independent of the Cu/Au stoichiometric ratios (Figures 5A and 5B). The modest but discernible differences between the experimentally measured (Figure 5A) and DDA-calculated (Figure 5B) extinction spectral features were primarily caused by the nonideality in the particle shapes of experimentally synthesized samples. As an increasing amount of Cu was incorporated into the alloy matrices, the particle morphology deviated from the ideal spherical shape to a greater extent (see TEM images in Figure S5 in the Supporting Information), giving rise to the slight redshift and weakening of the plasmon peak observed in Figure 5A. The results of DDA calculations further revealed that the light absorption efficiencies increased sharply above the onset of the interband transitions, while the extinction spectral features at the plasmon resonance wavelengths were dominated by scattering (Figure S16 in the Supporting Information). As the Cu/Au stoichiometric ratio increased, the energy threshold for interband transitions was red-shifted from ∼520 nm for Au to ∼590 nm for Cu. The detailed kinetic results of the reactions catalyzed by $AuCu_{4.2}$-142, $AuCu_{2.2}$-138, $AuCu_{0.83}$-140, $AuCu_{0.27}$-141, and Au-139 under various photoexcitation conditions were shown in Figure 5C−5E. For the interband hot carrier-driven reactions at λ_{ex}s of 445 (Figure 5F) and 520 nm (Figure 5G), k increased with Cu/Au atomic ratio, whereas a volcano-type relationship between k and Cu/Au atomic ratio was observed in the case of intraband hot carrier-driven reactions at λ_{ex} of 638 nm (Figure 5H),

https://doi.org/10.1021/acsnanoscienceau.4c00035
ACS Nanosci. Au 2024, 4, 360−373

achieving the maximal k value at a Cu/Au atomic ratio of 0.83. As revealed by DDA calculations, the light absorption efficiencies of these 140 nm-large alloy nanoparticles at 445, 520, and 638 nm were almost independent of the Cu/Au atomic ratios (Figure S16 in the Supporting Information). DDA calculations also showed that the local field enhancements at various λ_{ex}s remained almost unchanged as the Cu/Au stoichiometric ratios varied (Figure S17 in the Supporting Information). Therefore, the composition-dependency of k that we experimentally observed should not be explained as the consequence of different absorption efficiencies or local-field enhancements. The origin of the dependence of k on the Cu/Au stoichiometric ratio could be more reasonably interpreted in the context of hot carrier lifetimes and energetics, both of which depended on alloy compositions. Variation of the surface Cu/Au atomic ratios may also affect the metal-adsorbate interactions, which further influences the overall photocatalytic activity of the alloy nanoparticles. How the variation of Cu/Au stoichiometric ratios modifies the properties of interband and intraband hot carriers in alloy nanoparticles and the interactions between molecular adsorbates and nanoparticles deserves further investigations at a higher level of depth and quantitativeness.

With H_2O_2 serving as the electron acceptors, the interband hot carriers, including both electrons and holes, could be harnessed to produce $OH^{\bullet}$ radicals (Figure 2A), which caused the degradation of RhB. As illustrated in Figure 6A, in the absence of H_2O_2, the energetic interband hot holes in the d band were still exploitable for generating the reactive $OH^{\bullet}$ radicals, while the less energetic interband electrons in the *sp* band were probably utilized to drive hydrogen evolution from water (standard reduction potential of H_2O/H_2: −4.5 eV vs vacuum). In a H_2O_2-free environment, the photocatalytic degradation of RhB at λ_{ex} of 445 nm was driven solely by interband hot holes and became kinetically slower than their counterparts driven by both electrons and holes in the presence of H_2O_2 (Figure 6B). In the presence of $OH^{\bullet}$ radical scavengers, such as TBA, the interband hot hole-driven RhB degradation could be completely suppressed (Figure S18 in the Supporting Information). The results of control experiments conducted on N_2- and O_2-purged reactant−catalyst mixtures in a H_2O_2-free environment (Figure S19 in the Supporting Information) strongly suggested that the RhB degradation was driven by $OH^{\bullet}$ rather than $O_2^{\bullet-}$, another possibly existing ROS produced upon injection of hot electrons into the dissolved O_2 in the aqueous reaction medium. In the absence of H_2O_2, we did not observe any RhB degradation at an λ_{ex} of 638 nm (Figure 6B), as the intraband hot holes were energetically insufficient to drive the oxidation of water into $OH^{\bullet}$ radicals. By fitting the kinetic results collected from $AuCu_{4.2}$-142, $AuCu_{2.2}$-138, $AuCu_{0.83}$-140, $AuCu_{0.27}$-141, and Au-139 at λ_{ex} of 445 nm and P_{ex} of 0.5 W under H_2O_2-free reaction conditions (Figure S20 in the Supporting Information), the rate constants for the interband hole-driven reactions, k_{h+}, were obtained and plotted as a function of Cu/Au atomic ratio in Figure 6C. We further compared the rates of hole-driven reactions in H_2O_2-free environments to those of the reactions driven by both electrons and holes in the presence of H_2O_2. The ratio of k_{h+}/k reflected the relative contributions of interband hot holes and electrons to the overall rates of the photocatalytic reactions. As shown in Figure 6D, alloying Au with Cu led to decreased k_{h+}/k values, which could be interpreted in the context of composition-dependent energy shifts of the work function and d band in the Au−Cu alloys. Increasing the Cu/Au stoichiometric ratio led to a decrease in the alloy's work function within the range from 5.1 eV (Au) to 4.7 eV (Cu).[33,55] Consequently, the energy distributions of the interband hot electrons were upshifted with respect to the LUMO of H_2O_2, facilitating the metal-to-H_2O_2 transfer of hot electrons. Meanwhile, the d band was also shifted toward the Fermi level as the alloy nanoparticles became more Cu-rich, making the interband hot holes less energetic and oxidative in nature. The detailed relationships between the Fermi energy and the Au/Cu stoichiometry still need to be investigated at a higher level of quantitativeness through combined experimental and computational efforts, which will ultimately allow us to better understand the hybridization of electronic bands in alloy nanoparticle systems.

Photothermal Transduction in Au−Cu Alloy Nanoparticles

Photoexcited hot carriers, both interband and intraband, either got injected into molecular adsorbates to drive photocatalytic reactions or underwent relaxation and thermalization processes through electron−electron, electron−surface, and electron−phonon interactions within the nanoparticles.[2] The thermalization of hot carriers eventually led to a temperature elevation in the metal lattices followed by heat dissipation to the surroundings. Photothermal transduction could be considered as a process competing with the metal-to-adsorbate transfer of hot carriers. Here, we studied the photothermal properties of a series of monometallic Au and composition-varying Au−Cu alloy nanoparticles, all of which had average particle sizes around 140 nm ($AuCu_{4.2}$-142, $AuCu_{2.2}$-138, $AuCu_{0.83}$-140, $AuCu_{0.27}$-141, and Au-139). We monitored the temperature evolutions of 2.0 mL of aqueous suspensions of colloidal particles at a concentration of 1.0×10^9 particles mL^{-1} under continuous laser illumination at λ_{ex}s of 445, 520, and 638 nm in ambient air (Figure S21 in the Supporting Information). After the thermal equilibrium was reached, the illumination laser was turned off, and the colloidal suspensions were naturally cooled to room temperature under ambient air. The photothermal results were analyzed using a thermophysical model previously reported by Roper and co-workers.[78] The values of the thermal equilibrium time constant, τ_s, were obtained by fitting the temperature evolution in the cooling processes (Figure S22 in Supporting Information) with the following equation:

$$\ln\left(\frac{T - T_0}{T_{eq} - T_0}\right) = \ln\left(\frac{\Delta T}{\Delta T_{eq}}\right) = -\frac{1}{\tau_s} \times t \tag{4}$$

where T_0 is the ambient temperature and T_{eq} is the steady state temperature reached at thermal equilibrium under continuous laser illumination. Considering the balanced energy flow at the thermal equilibrium, the photothermal transduction efficiency, ϕ, could be calculated using the following equation (see more details in the Supporting Information):

$$\varphi = \frac{m_{water} C_{p,water}\left(\frac{1}{\tau_s}\Delta T_{eq} - \frac{1}{\tau_{s,water}}\Delta T_{eq,water}\right)}{P_{ex}(1 - 10^{-A_\lambda})} \tag{5}$$

in which m_{water} and $C_{p,water}$ are the mass and constant-pressure heat capacity of water (m_{water} = 2.0 g and $C_{p,water}$ = 4.184 J K^{-1} g^{-1}), respectively. $\tau_{s,water}$ and $\Delta T_{eq,water}$ refer to the τ_s and ΔT_{eq} for pure water without any colloidal nanoparticles. A_λ is the

https://doi.org/10.1021/acsnanoscienceau.4c00035
ACS Nanosci. Au 2024, 4, 360−373

absorbance at the excitation wavelength with an optical path length of 2 cm. As shown in Figure S23 in the Supporting Information, the ϕ values under plasmonic excitations at λ_{ex}s of 638 nm were significantly higher than those under interband excitations at λ_{ex}s of 445 and 520 nm. Although the ϕ values increased with the Cu/Au stoichiometric ratios under intraband plasmonic excitations, they became almost independent of the alloy compositions under interband excitations. These results suggested that the intraband hot carriers derived from plasmon decay were less active for photocatalysis but more efficient for photothermal transduction in comparison to the interband hot carriers.

CONCLUSIONS

Au−Cu alloy nanoparticles represent a unique materials system in which the Cu/Au stoichiometric ratios determine the threshold of excitation energy for *d*-to-*sp* interband electronic transitions, while the resonant frequencies of the dipole plasmons can be tuned by varying the particle sizes. The degree of spectral overlap between plasmon resonances and interband transitions in the visible spectral region regulates the interband damping of plasmons, which profoundly influences the relative populations, energy distributions, and photocatalytic efficacies of intraband and interband hot carriers in Au−Cu alloy nanoparticles. Using photocatalytic degradation of RhB as a model reaction, we have systematically compared the photocatalytic efficacies of interband and intraband hot carriers in Au−Cu alloy nanoparticles with finely tunable compositional stoichiometries over a broad range of particle sizes across the quasi-static limit. The photocatalytic action spectra match the extinction spectral profiles very well in the case of small monometallic Au nanoparticles within the quasi-static limit. However, increasing the particle sizes or alloying Au with Cu leads to drastically enhanced photocatalytic efficacies of interband hot carriers, causing the photocatalytic action spectra to deviate significantly from the optical extinction spectra. In Au−Cu alloy nanoparticles over the entire range of stoichiometric ratios and particle sizes investigated in this work, the interband hot carriers have been observed to be photocatalytically more active than the intraband hot carriers derived from nonradiative plasmon decay. In relatively large nanoparticles beyond the quasi-static limit, diffusion of hot carriers inside the nanoparticles becomes a critical factor limiting the surface abundance and utilization efficiencies of hot carriers for photocatalysis. At a fixed Cu/Au stoichiometric ratio, the surface-specific rate constants of the photocatalytic reactions driven by intraband hot carriers decay more rapidly than those of interband hot carrier-driven reactions upon increase of particle size, implying that interband hot carriers are longer-lived and can diffuse over longer distances in comparison to the intraband hot carriers. At a given particle size, the reaction rate increases monotonically with the Cu/Au atomic ratio under interband excitations but switches to a volcano-type composition dependence in the case of intraband hot carrier-driven reactions. The experimentally observed composition-dependence of reaction rate can be most reasonably interpreted in the context of composition-dependent lifetimes and energy distributions of hot carriers. The insights gained from this work provide a critical knowledge foundation for deciphering the effects of particle dimensions and compositional stoichiometries on the photoexcitation efficiencies and photocatalytic efficacies of interband and intraband hot carriers in multimetallic alloy nanoparticles.

METHODS

Synthesis and Characterizations of Nanoparticles

Colloidal nanoparticles made of Au and Au−Cu alloys with precisely tunable particle sizes and Cu/Au stoichiometric ratios were synthesized following previously published protocols.[43,44] The particle sizes, crystalline structures, chemical compositions, and optical properties of the monometallic Au and bimetallic Au−Cu alloy nanoparticles were characterized using TEM, PXRD, EDS, and optical extinction spectroscopy, respectively. Experimental details associated with nanoparticle syntheses and characterizations are presented in the Supporting Information.

Photocatalytic RhB Degradation

The photocatalytic performances of Au and Au−Cu alloy nanoparticles under continuous laser illuminations at various λ_{ex}s and P_{ex}s were evaluated through detailed kinetic studies of photocatalytic degradation of RhB with H_2O_2 serving as an electron acceptor. Colloidal Au or Au−Cu alloy nanoparticles were first mixed with RhB in aqueous solutions at a pH of 7.0 in a quartz cuvette (1.0 × 1.0 × 4.5 cm). The concentrations of colloidal nanoparticles and RhB molecules in the reaction mixtures were ∼1.0×10^9 particles mL^{-1} and 2.0 μM, respectively. The total volume of the reaction mixtures was kept at 2.0 mL. Prior to the laser illumination, the mixtures were kept in the dark under magnetic stirring for 4 h to achieve a pre-established adsorption/desorption equilibrium. After introducing 2 μL of 2 M H_2O_2 into the reaction mixture, the photocatalytic reactions were initiated upon illumination by an excitation laser. Five continuous wave (cw) diode lasers purchased from Lasever Inc. (Ningbo, Zhejiang, China) with a tunable power output in the range of 0−3.0 W and emission wavelengths at 445 nm (model no. LSR445SD), 520 nm (model no. LSR520CPD), 638 nm (model no. LSR638CP8), 785 nm (model no. LSR785NL), and 980 nm (model no. LSR980NL) were used as light sources for excitations. The excitation lasers were collimated with a 4 × 4 mm square-shaped cross section and incident vertically from the top surface into the solution-containing cuvettes. The catalyst−reactant mixtures were kept under magnetic stirring (200 rpm), and the cuvette was immersed in a large water bath (4 L in volume) to facilitate the dissipation of photothermally generated heat. To monitor the reaction progress, the RhB molecules remaining in the solution were separated from the photocatalysts through centrifugation every 10 min during the reactions, and UV−visible absorption spectra were collected using a Beckman Coulter Du 640 spectrophotometer. The characteristic absorption peak of RhB was centered at 553 nm, and the absorbance at 553 nm was used to quantify the RhB concentration. The photocatalysts were then remixed with the remaining RhB molecules and subjected to further photocatalytic reactions upon exposure to laser illumination. To test the photocatalytic durability, the photocatalysts were recycled through centrifugation after the photoreactions proceeded for 20 min and then redispersed in 2 mL solution containing 2.0 μM RhB and 2 mM H_2O_2 for the next reaction cycle.

Photothermal Measurements

To study the photothermal properties of Au and Au−Cu alloy nanoparticles, we monitored the temperature evolution of 2.0 mL of aqueous colloidal suspensions under continuous laser illumination. After reaching thermal equilibrium, the colloidal suspensions were naturally cooled to ambient temperature in the dark. The solution-phase temperature was monitored as a function of time, *t*, over multiple cycles of laser illumination and natural cooling using a digital thermocouple (Therma Waterproof Thermometer for Type K Thermocouples, Priggen Special Electronic). The photothermal results were analyzed using a thermophysical model previously reported by Roper and co-workers.[78] A detailed description of the photothermal measurements and analysis is presented in the Supporting Information.

Discrete Dipole Approximation (DDA) Calculations

The DDA method was used to calculate the extinction, absorption, and scattering spectra of Au−Cu alloy nanoparticles as well as the

https://doi.org/10.1021/acsnanoscienceau.4c00035
ACS Nanosci. Au 2024, 4, 360−373

local field enhancements near the nanoparticle surfaces.[79] Each spherical Au, Cu, or alloy nanoparticle was divided into polarizable cubes, and the coupling among these cubes and incident light was modeled using the coupled dipole method. The edge length of each cube was set at 1 nm. The dielectric constants of Au and Cu were taken from Johnson and Christy's work.[46] For alloy nanoparticles, the number of cubes for each component was proportional to their corresponding atomic ratio as determined experimentally, and the Au and Cu cubes were randomly distributed in each alloy nanoparticle.

■ ASSOCIATED CONTENT

Supporting Information

The Supporting Information is available free of charge at https://pubs.acs.org/doi/10.1021/acsnanoscienceau.4c00035.

Additional experimental details and additional figures as noted in the maintext, including dielectric functions of Au and Cu, calculated extinction, absorption, and scattering spectra, PXRD pattern, TEM images, EDS-based elemental analysis, detailed kinetic results of photocatalytic reactions, temperature evolutions under continuous laser illumination, DDA-calculated local field enhancements, and photothermal transduction efficiencies (PDF)

■ AUTHOR INFORMATION

Corresponding Author

Hui Wang − *Department of Chemistry and Biochemistry, University of South Carolina, Columbia, South Carolina 29208, United States;* orcid.org/0000-0002-1874-5137; Phone: 1-803-777-2203; Email: wang344@mailbox.sc.edu

Authors

Mengqi Sun − *Department of Chemistry and Biochemistry, University of South Carolina, Columbia, South Carolina 29208, United States*

Ankai Wang − *Department of Chemistry, University of Central Florida, Orlando, Florida 32816, United States*

Min Zhang − *Department of Chemistry and Biochemistry, University of South Carolina, Columbia, South Carolina 29208, United States*

Shengli Zou − *Department of Chemistry, University of Central Florida, Orlando, Florida 32816, United States;* orcid.org/0000-0003-1302-133X

Complete contact information is available at: https://pubs.acs.org/10.1021/acsnanoscienceau.4c00035

Author Contributions

M.S. synthesized the materials, characterized the nanostructures, and studied the photocatalytic reaction kinetics. A.W. did the DDA calculations. M.Z. characterized the materials. M.S., M.Z., and H.W. analyzed the data. H.W. and M.S. wrote the paper with contributions from all authors. H.W. and S.Z. designed the project, supervised the research, and acquired funding support. All authors have given approval to the final version of the manuscript.

Notes

The authors declare no competing financial interest.

■ ACKNOWLEDGMENTS

The work done at University of South Carolina (UofSC) was supported by the National Science Foundation (NSF) under Grants OIA-1655740 and CHE-2202928. The work done at the University of Central Florida was supported by NSF under grant CBET-2230891. This work made use of the X-ray diffraction facilities at the South Carolina SAXS Collaborative supported by the NSF MRI program (DMR-1428620) and the electron microscopy facilities at the UofSC Electron Microscopy Center. The instrument used for EDS elemental analysis was purchased using the South Carolina STEM Equipment Funds.

■ REFERENCES

(1) Linic, S.; Christopher, P.; Ingram, D. B. Plasmonic-Metal Nanostructures for Efficient Conversion of Solar to Chemical Energy. *Nat. Mater.* **2011**, *10* (12), 911−921.

(2) Brongersma, M. L.; Halas, N. J.; Nordlander, P. Plasmon-Induced Hot Carrier Science and Technology. *Nature Nanotechnology* **2015**, *10* (1), 25−34.

(3) Kale, M. J.; Avanesian, T.; Christopher, P. Direct Photocatalysis by Plasmonic Nanostructures. *ACS Catalysis* **2014**, *4* (1), 116−128.

(4) Zhang, Y. C.; He, S.; Guo, W. X.; Hu, Y.; Huang, J. W.; Mulcahy, J. R.; Wei, W. D. Surface-Plasmon-Driven Hot Electron Photochemistry. *Chemical Reviews* **2018**, *118* (6), 2927−2954.

(5) Christopher, P.; Moskovits, M., Hot Charge Carrier Transmission from Plasmonic Nanostructures. In *Annual Review of Physical Chemistry*, Johnson, M. A.; Martinez, T. J., Eds. 2017; Vol. *68*, pp 379-398.

(6) Kazuma, E.; Kim, Y. Mechanistic Studies of Plasmon Chemistry on Metal Catalysts. *Angewandte Chemie-International Edition* **2019**, *58* (15), 4800−4808.

(7) Govorov, A. O.; Zhang, H.; Demir, H. V.; Gun'ko, Y. K. Photogeneration of Hot Plasmonic Electrons with Metal Nanocrystals: Quantum Description and Potential Applications. *Nano Today* **2014**, *9* (1), 85−101.

(8) Brown, A. M.; Sundararaman, R.; Narang, P.; Goddard, W. A.; Atwater, H. A. Nonradiative Plasmon Decay and Hot Carrier Dynamics: Effects of Phonons, Surfaces, and Geometry. *ACS Nano* **2016**, *10* (1), 957−966.

(9) Minutella, E.; Schulz, F.; Lange, H. Excitation-Dependence of Plasmon-Induced Hot Electrons in Gold Nanoparticles. *Journal of Physical Chemistry Letters* **2017**, *8* (19), 4925−4929.

(10) Zhao, J.; Nguyen, S. C.; Ye, R.; Ye, B. H.; Weller, H.; Somorjai, G. A.; Alivisatos, A. P.; Toste, F. D. A Comparison of Photocatalytic Activities of Gold Nanoparticles Following Plasmonic and Interband Excitation and a Strategy for Harnessing Interband Hot Carriers for Solution Phase Photocatalysis. *ACS Central Science* **2017**, *3* (5), 482−488.

(11) Lyu, P.; Espinoza, R.; Nguyen, S. C. Photocatalysis of Metallic Nanoparticles: Interband *vs* Intraband Induced Mechanisms. *Journal of Physical Chemistry C* **2023**, *127* (32), 15685−15698.

(12) Jin, H.; Kahk, J. M.; Papaconstantopoulos, D. A.; Ferreira, A.; Lischner, J. Plasmon-Induced Hot Carriers from Interband and Intraband Transitions in Large Noble Metal Nanoparticles. *PRX Energy* **2022**, *1* (1), No. 013006.

(13) Tagliabue, G.; DuChene, J. S.; Habib, A.; Sundararaman, R.; Atwater, H. A. Hot-Hole versus Hot-Electron Transport at Cu/GaN Heterojunction Interfaces. *ACS Nano* **2020**, *14* (5), 5788−5797.

(14) Tagliabue, G.; Jermyn, A. S.; Sundararaman, R.; Welch, A. J.; DuChene, J. S.; Pala, R.; Davoyan, A. R.; Narang, P.; Atwater, H. A. Quantifying the Role of Surface Plasmon Excitation and Hot Carrier Transport in Plasmonic Devices. *Nat. Commun.* **2018**, *9* (1), 3394.

(15) Fu, X. Q.; Li, G. G.; Villarreal, E.; Wang, H. Hot Carriers in Action: Multimodal Photocatalysis on Au@SnO_2 Core-Shell Nanoparticles. *Nanoscale* **2019**, *11* (15), 7324−7334.

(16) Kim, Y.; Smith, J. G.; Jain, P. K. Harvesting Multiple Electron-Hole Pairs Generated through Plasmonic Excitation of Au Nanoparticles. *Nature Chemistry* **2018**, *10* (7), 763−769.

(17) Stofela, S. K. F.; Kizilkaya, O.; Diroll, B. T.; Leite, T. R.; Taheri, M. M.; Willis, D. E.; Baxter, J. B.; Shelton, W. A.; Sprunger, P. T.;

McPeak, K. M. A Noble-Transition Alloy Excels at Hot-Carrier Generation in the Near Infrared. *Adv. Mater.* **2020**, *32* (23), No. 1906478.
(18) Zhou, L.; Zhang, C.; McClain, M. J.; Manjavacas, A.; Krauter, C. M.; Tian, S.; Berg, F.; Everitt, H. O.; Carter, E. A.; Nordlander, P.; Halas, N. J. Aluminum Nanocrystals as a Plasmonic Photocatalyst for Hydrogen Dissociation. *Nano Letters* **2016**, *16* (2), 1478−1484.
(19) Blaber, M. G.; Arnold, M. D.; Ford, M. J. A Review of the Optical Properties of Alloys and Intermetallics for Plasmonics. *Journal of Physics-Condensed Matter* **2010**, *22* (14), 143201.
(20) Sytwu, K.; Vadai, M.; Dionne, J. A. Bimetallic Nanostructures: Combining Plasmonic and Catalytic Metals for Photocatalysis. *Advances in Physics-X* **2019**, *4* (1), 1619480.
(21) Zaleska-Medynska, A.; Marchelek, M.; Diak, M.; Grabowska, E. Noble Metal-Based Bimetallic Nanoparticles: The Effect of the Structure on the Optical, Catalytic and Photocatalytic Properties. *Adv. Colloid Interface Sci.* **2016**, *229*, 80−107.
(22) Li, K.; Hogan, N. J.; Kale, M. J.; Halas, N. J.; Nordlander, P.; Christopher, P. Balancing Near-Field Enhancement, Absorption, and Scattering for Effective Antenna-Reactor Plasmonic Photocatalysis. *Nano Letters* **2017**, *17* (6), 3710−3717.
(23) Robatjazi, H.; Zhao, H.; Swearer, D. F.; Hogan, N. J.; Zhou, L.; Alabastri, A.; McClain, M. J.; Nordlander, P.; Halas, N. J. Plasmon-Induced Selective Carbon Dioxide Conversion on Earth-Abundant Aluminum-Cuprous Oxide Antenna-Reactor Nanoparticles. *Nat. Commun.* **2017**, *8*, 27.
(24) Swearer, D. F.; Zhao, H. Q.; Zhou, L. N.; Zhang, C.; Robatjazi, H.; Martirez, J. M. P.; Krauter, C. M.; Yazdi, S.; McClain, M. J.; Ringe, E.; Carter, E. A.; Nordlander, P.; Halas, N. J. Heterometallic Antenna-Reactor Complexes for Photocatalysis. *Proceedings of the National Academy of Sciences of the United States of America* **2016**, *113* (32), 8916−8920.
(25) Zhang, C.; Zhao, H. Q.; Zhou, L. A.; Schlather, A. E.; Dong, L. L.; McClain, M. J.; Swearer, D. F.; Nordlander, P.; Halas, N. J. Al-Pd Nanodisk Heterodimers as Antenna-Reactor Photocatalysts. *Nano Letters* **2016**, *16* (10), 6677−6682.
(26) Zhou, L. A.; Martirez, J. M. P.; Finzel, J.; Zhang, C.; Swearer, D. F.; Tian, S.; Robatjazi, H.; Lou, M. H.; Dong, L. L.; Henderson, L.; Christopher, P.; Carter, E. A.; Nordlander, P.; Halas, N. J. Light-Driven Methane Dry Reforming with Single Atomic Site Antenna-Reactor Plasmonic Photocatalysts. *Nature Energy* **2020**, *5* (1), 61−70.
(27) Zhu, Z.; Tang, R.; Li, C.; An, X.; He, L. Promises of Plasmonic Antenna-Reactor Systems in Gas-Phase CO_2 Photocatalysis. *Adv. Sci.* **2023**, *10* (24), No. 2302568.
(28) Wang, Z. X.; Wang, H. Au@C/Pt Core@Shell/Satellite Supra-Nanostructures: Plasmonic Antenna-Reactor Hybrid Nanocatalysts. *Nanoscale Advances* **2023**, *5* (20), 5435−5448.
(29) Zhu, X.; Jia, H.; Zhu, X.; Cheng, S.; Zhuo, X.; Qin, F.; Yang, Z.; Wang, J. Selective Pd Deposition on Au Nanobipyramids and Pd Site-Dependent Plasmonic Photocatalytic Activity. *Adv. Funct. Mater.* **2017**, *27* (22), No. 1700016.
(30) Valenti, M.; Venugopal, A.; Tordera, D.; Jonsson, M. P.; Biskos, G.; Schmidt-Ott, A.; Smith, W. A. Hot Carrier Generation and Extraction of Plasmonic Alloy Nanoparticles. *ACS Photonics* **2017**, *4* (5), 1146−1152.
(31) Wang, J. L.; Ando, R. A.; Camargo, P. H. C. Investigating the Plasmon-Mediated Catalytic Activity of AgAu Nanoparticles as a Function of Composition: Are Two Metals Better Than One? *ACS Catalysis* **2014**, *4* (11), 3815−3819.
(32) Gong, C.; Kaplan, A.; Benson, Z. A.; Baker, D. R.; McClure, J. P.; Rocha, A. R.; Leite, M. S. Band Structure Engineering by Alloying for Photonics. *Adv. Opt. Mater.* **2018**, *6* (17), No. 1800218.
(33) Lee, C.; Park, Y.; Park, J. Y. Hot Electrons Generated by Intraband and Interband Transition Detected Using a Plasmonic Cu/TiO_2 Nanodiode. *RSC Advances* **2019**, *9* (32), 18371−18376.
(34) Zheng, P.; Tang, H. B.; Liu, B. T.; Kasani, S.; Huang, L.; Wu, N. Q. Origin of Strong and Narrow Localized Surface Plasmon Resonance of Copper Nanocubes. *Nano Research* **2019**, *12* (1), 63−68.
(35) Wang, H.; Tam, F.; Grady, N. K.; Halas, N. J. Cu Nanoshells: Effects of Interband Transitions on the Nanoparticle Plasmon Resonance. *Journal of Physical Chemistry B* **2005**, *109* (39), 18218−18222.
(36) Chan, G. H.; Zhao, J.; Hicks, E. M.; Schatz, G. C.; Van Duyne, R. P. Plasmonic Properties of Copper Nanoparticles Fabricated by Nanosphere Lithography. *Nano Letters* **2007**, *7* (7), 1947−1952.
(37) Xu, Z. C.; Lai, E. C.; Shao-Horn, Y.; Hamad-Schifferli, K. Compositional Dependence of the Stability of AuCu Alloy Nanoparticles. *Chemical Communications* **2012**, *48* (45), 5626−5628.
(38) Schaak, R. E.; Sra, A. K.; Leonard, B. M.; Cable, R. E.; Bauer, J. C.; Han, Y. F.; Means, J.; Teizer, W.; Vasquez, Y.; Funck, E. S. Metallurgy in a Beaker: Nanoparticle Toolkit for the Rapid Low-Temperature Solution Synthesis of Functional Multimetallic Solid-State Materials. *J. Am. Chem. Soc.* **2005**, *127* (10), 3506−3515.
(39) Motl, N. E.; Ewusi-Annan, E.; Sines, I. T.; Jensen, L.; Schaak, R. E. Au-Cu Alloy Nanoparticles with Tunable Compositions and Plasmonic Properties: Experimental Determination of Composition and Correlation with Theory. *Journal of Physical Chemistry C* **2010**, *114* (45), 19263−19269.
(40) Li, G. G.; Villarreal, E.; Zhang, Q. F.; Zheng, T. T.; Zhu, J. J.; Wang, H. Controlled Dealloying of Alloy Nanoparticles toward Optimization of Electrocatalysis on Spongy Metallic Nanoframes. *ACS Applied Materials & Interfaces* **2016**, *8* (36), 23920−23931.
(41) Li, G. G.; Lin, Y.; Wang, H. Residual Silver Remarkably Enhances Electrocatalytic Activity and Durability of Dealloyed Gold Nanosponge Particles. *Nano Letters* **2016**, *16* (11), 7248−7253.
(42) Kim, D.; Resasco, J.; Yu, Y.; Asiri, A. M.; Yang, P. D. Synergistic Geometric and Electronic Effects for Electrochemical Reduction of Carbon Dioxide Using Gold-Copper Bimetallic Nanoparticles. *Nature Communications* **2014**, *5*, 4948.
(43) Sun, M. Q.; Wang, Z. X.; Wang, H. Chemically Driven Phase Segregation of Alloy Nanoparticles: A Versatile Route to Dual-Plasmonic Gold@Copper Chalcogenide Heteronanostructures. *Chem. Mater.* **2022**, *34* (4), 1965−1975.
(44) Li, G. G.; Sun, M. Q.; Villarreal, E.; Pandey, S.; Phillpot, S. R.; Wang, H. Galvanic Replacement-Driven Transformations of Atomically Intermixed Bimetallic Colloidal Nanocrystals: Effects of Compositional Stoichiometry and Structural Ordering. *Langmuir* **2018**, *34* (14), 4340−4350.
(45) Bohren, C. F.; Huffman, D. R.; *Absorption and Scattering of Light by Small Particles*. John Wiley & Sons: New York, 1983.
(46) Johnson, P. B.; Christy, R. W. Optical Constants of the Noble Metals. *Physical Review B* **1972**, *6* (12), 4370−4379.
(47) Ziegler, C.; Eychmüller, A. Seeded Growth Synthesis of Uniform Gold Nanoparticles with Diameters of 15−300 nm. *The Journal of Physical Chemistry C* **2011**, *115* (11), 4502−4506.
(48) Bastús, N. G.; Comenge, J.; Puntes, V. Kinetically Controlled Seeded Growth Synthesis of Citrate-Stabilized Gold Nanoparticles of up to 200 nm: Size Focusing Versus Ostwald Ripening. *Langmuir* **2011**, *27* (17), 11098−11105.
(49) Pacioni, N. L.; Filippenko, V.; Presseau, N.; Scaiano, J. C. Oxidation of Copper Nanoparticles in Water: Mechanistic Insights Revealed by Oxygen Uptake and Spectroscopic Methods. *Dalton Transactions* **2013**, *42* (16), 5832−5838.
(50) Park, B. K.; Jeong, S.; Kim, D.; Moon, J.; Lim, S.; Kim, J. S. Synthesis and Size Control of Monodisperse Copper Nanoparticles by Polyol Method. *J. Colloid Interface Sci.* **2007**, *311* (2), 417−424.
(51) Zhang, P. N.; Li, Y. J.; Wang, D. Y.; Xia, H. B. High-Yield Production of Uniform Gold Nanoparticles with Sizes from 31 to 577 nm *via* One-Pot Seeded Growth and Size-Dependent SERS Property. *Part Part Syst Char* **2016**, *33* (12), 924−932.
(52) Zhang, L.; Jing, H.; Boisvert, G.; He, J. Z.; Wang, H. Geometry Control and Optical Tunability of Metal−Cuprous Oxide Core−Shell Nanoparticles. *ACS Nano* **2012**, *6* (4), 3514−3527.
(53) Vegard, L. The Constitution of the Mixed Crystals and the Filling of Space of the Atoms. *Zeitsch rift fiir Physics* **1921**, *5*, 17−23.
(54) Lubarda, V. A. On the Effective Lattice Parameter of Binary Alloys. *Mechanics of Materials* **2003**, *35* (1−2), 53−68.

https://doi.org/10.1021/acsnanoscienceau.4c00035
ACS Nanosci. Au 2024, 4, 360−373

(55) Lombardi, J. R.; Birke, R. L. A Unified Approach to Surface-Enhanced Raman Spectroscopy. *Journal of Physical Chemistry C* **2008**, *112* (14), 5605−5617.
(56) Hoffmann, M. R.; Martin, S. T.; Choi, W. Y.; Bahnemann, D. W. Environmental Applications of Semiconductor Photocatalysis. *Chemical Reviews* **1995**, *95* (1), 69−96.
(57) Garcia-Segura, S.; Brillas, E. Applied Photoelectrocatalysis on the Degradation of Organic Pollutants in Wastewaters. *Journal of Photochemistry and Photobiology C-Photochemistry Reviews* **2017**, *31*, 1−35.
(58) Maeda, K. Photocatalytic Water Splitting Using Semiconductor Particles: History and Recent Developments. *Journal of Photochemistry and Photobiology C: Photochemistry Reviews* **2011**, *12* (4), 237−268.
(59) McMichael, S.; Fernández-Ibáñez, P.; Byrne, J. A. A Review of Photoelectrocatalytic Reactors for Water and Wastewater Treatment. *Water* **2021**, *13* (9), 1198.
(60) Zhang, Y.; Villarreal, E.; Li, G. G.; Wang, W.; Wang, H. Plasmonic Nanozymes: Engineered Gold Nanoparticles Exhibit Tunable Plasmon-Enhanced Peroxidase-Mimicking Activity. *Journal of Physical Chemistry Letters* **2020**, *11* (21), 9321−9328.
(61) Sang, X. Q.; Xia, S. Y.; Cheng, L.; Wu, F. X.; Tian, Y.; Guo, C. X.; Xu, G. B.; Yuan, Y. L.; Niu, W. X. Deciphering the Mechanisms of Photo-Enhanced Catalytic Activities in Plasmonic Pd-Au Heteromeric Nanozymes for Colorimetric Analysis. *Small* **2024**, *20* (3), No. 2305369.
(62) Wang, C.; Shi, Y.; Dan, Y. Y.; Nie, X. G.; Li, J.; Xia, X. H. Enhanced Peroxidase-Like Performance of Gold Nanoparticles by Hot Electrons. *Chemistry-a European Journal* **2017**, *23* (28), 6717−6723.
(63) Dabera, G. D. M. R.; Walker, M.; Sanchez, A. M.; Pereira, H. J.; Beanland, R.; Hatton, R. A. Retarding Oxidation of Copper Nanoparticles without Electrical Isolation and the Size Dependence of Work Function. *Nat. Commun.* **2017**, *8* (1), 1894.
(64) Du, T.; Vijayakumar, A.; Desai, V. Effect of Hydrogen Peroxide on Oxidation of Copper in CMP Slurries Containing Glycine and Cu Ions. *Electrochim. Acta* **2004**, *49* (25), 4505−4512.
(65) Kazuma, E.; Jung, J.; Ueba, H.; Trenary, M.; Kim, Y. Direct Pathway to Molecular Photodissociation on Metal Surfaces Using Visible Light. *J. Am. Chem. Soc.* **2017**, *139* (8), 3115−3121.
(66) Kazuma, E.; Jung, J.; Ueba, H.; Trenary, M.; Kim, Y. Real-Space and Real-Time Observation of a Plasmon-Induced Chemical Reaction of a Single Molecule. *Science* **2018**, *360* (6388), 521−526.
(67) Tesema, T. E.; Kafle, B.; Habteyes, T. G. Plasmon-Driven Reaction Mechanisms: Hot Electron Transfer versus Plasmon-Pumped Adsorbate Excitation. *The Journal of Physical Chemistry C* **2019**, *123* (14), 8469−8483.
(68) Miliutina, E.; Guselnikova, O.; Soldatova, N. S.; Bainova, P.; Elashnikov, R.; Fitl, P.; Kurten, T.; Yusubov, M. S.; Švorčík, V.; Valiev, R. R.; Chehimi, M. M.; Lyutakov, O.; Postnikov, P. S. Can Plasmon Change Reaction Path? Decomposition of Unsymmetrical Iodonium Salts as an Organic Probe. *The Journal of Physical Chemistry Letters* **2020**, *11* (14), 5770−5776.
(69) Mukherjee, S.; Libisch, F.; Large, N.; Neumann, O.; Brown, L. V.; Cheng, J.; Lassiter, J. B.; Carter, E. A.; Nordlander, P.; Halas, N. J. Hot Electrons Do the Impossible: Plasmon-Induced Dissociation of H_2 on Au. *Nano Letters* **2013**, *13* (1), 240−247.
(70) Zhou, L. A.; Swearer, D. F.; Zhang, C.; Robatjazi, H.; Zhao, H. Q.; Henderson, L.; Dong, L. L.; Christopher, P.; Carter, E. A.; Nordlander, P.; Halas, N. J. Quantifying Hot Carrier and Thermal Contributions in Plasmonic Photocatalysis. *Science* **2018**, *362* (6410), 69−72.
(71) Baffou, G.; Bordacchini, I.; Baldi, A.; Quidant, R. Simple Experimental Procedures to Distinguish Photothermal from Hot-Carrier Processes in Plasmonics. *Light: Sci. Appl.* **2020**, *9* (1), 108.
(72) Christopher, P.; Xin, H. L.; Marimuthu, A.; Linic, S. Singular Characteristics and Unique Chemical Bond Activation Mechanisms of Photocatalytic Reactions on Plasmonic Nanostructures. *Nat. Mater.* **2012**, *11* (12), 1044−1050.
(73) Chen, K. X.; Wang, H. Origin of Superlinear Power Dependence of Reaction Rates in Plasmon-Driven Photocatalysis: A Case Study of Reductive Nitrothiophenol Coupling Reactions. *Nano Letters* **2023**, *23* (7), 2870−2876.
(74) Linic, S.; Aslam, U.; Boerigter, C.; Morabito, M. Photochemical Transformations on Plasmonic Metal Nanoparticles. *Nat. Mater.* **2015**, *14* (6), 567−576.
(75) Lyu, P.; Espinoza, R.; Khan, M. I.; Spaller, W. C.; Ghosh, S.; Nguyen, S. C. Mechanistic Insight into Deep Holes from Interband Transitions in Palladium Nanoparticle Photocatalysts. *iScience* **2022**, *25* (2), No. 103737.
(76) Zhai, Y.; DuChene, J. S.; Wang, Y.-C.; Qiu, J.; Johnston-Peck, A. C.; You, B.; Guo, W.; DiCiaccio, B.; Qian, K.; Zhao, E. W.; Ooi, F.; Hu, D.; Su, D.; Stach, E. A.; Zhu, Z.; Wei, W. D. Polyvinylpyrrolidone-Induced Anisotropic Growth of Gold Nanoprisms in Plasmon-Driven Synthesis. *Nat. Mater.* **2016**, *15* (8), 889−895.
(77) Mao, Z. L.; Vang, H.; Garcia, A.; Tohti, A.; Stokes, B. J.; Nguyen, S. C. Carrier Diffusion-the Main Contribution to Size-Dependent Photocatalytic Activity of Colloidal Gold Nanoparticles. *ACS Catalysis* **2019**, *9* (5), 4211−4217.
(78) Roper, D. K.; Ahn, W.; Hoepfner, M. Microscale Heat Transfer Transduced by Surface Plasmon Resonant Gold Nanoparticles. *Journal of Physical Chemistry C* **2007**, *111* (9), 3636−3641.
(79) Draine, B. T. The Discrete Dipole Approximation and Its Application to Interstellar Graphite Graines. *The Astrophysical Journal* **1988**, *333*, 848−872.

https://doi.org/10.1021/acsnanoscienceau.4c00035
ACS Nanosci. Au 2024, 4, 360−373